

From Pixels to Deposits: Porphyry Mineralization With Multispectral Convolutional Neural Networks

Usama Zidan , Hamdy A. El Desouky , Mohamed Medhat Gaber , and Mohammed M. Abdelsamea 

Abstract—Mineral exploration is essential to ensure a sustainable supply of raw materials for modern living and the transition to green. It implies a series of expensive operations that aim to identify areas with natural mineral concentration in the crust of the Earth. The rapid advances in artificial intelligence and remote sensing techniques can help in significantly reducing the cost of these operations. Here, we produce a robust intelligent mineral exploration model that can fingerprint potential locations of porphyry deposits, which are the world’s most important source of copper and molybdenum and major source of gold, silver, and tin. We present a deep learning pipeline for assessing multispectral imagery from the Advanced Spaceborne Thermal Emission and Reflection Radiometer (ASTER) with the objective of identifying hydrothermal alterations. Our approach leverages a convolutional neural network (CNN) to analyze the high-resolution images, overcoming computational challenges through a patch-based strategy that involves an overlapping window for partitioning the images into fixed-size patches. Through the utilization of manually labeled patches for image classification and identification of hydrothermal alteration areas, our results demonstrate the remarkable ability of CNN to accurately detect hydrothermal alterations. The technique is adaptable for other ore deposit models and satellite imagery types, providing a revolution in satellite image interpretation and mineral exploration.

Index Terms—Advanced Spaceborne Thermal Emission and Reflection Radiometer (ASTER), convolutional neural network (CNN), mineral exploration, multispectral image analysis.

I. INTRODUCTION

MINERAL exploration is critical to the long-term supply of raw materials required for modern living and the green transition. One important aspect of mineral exploration is the identification of hydrothermal alteration zones associated with porphyry copper deposits, which are the world’s most important source of copper and molybdenum, and major sources of gold, silver, and tin [1], [2], [3], [4]. Hydrothermal alteration zones

are footprints left by mineralizing fluids that have altered host rocks, resulting in changes in mineralogy, texture, and color. These changes can be detected by remote sensing techniques, such as satellite imagery, which can provide a cost-effective alternative to expensive and time-consuming regional mineral exploration. With a large number of satellites available in space, they scan the Earth’s surface at variable spatial and spectral resolutions. To deal with the large amount of data obtained from these satellites, there is an urgent need for intelligent rapid image interpretation techniques that would allow extracting the Earth’s features directly from raw data without intermediate image enhancement techniques. Artificial intelligence and machine learning (ML) techniques offer a promising solution to the challenge of interpreting the vast amount of data generated by remote sensing devices. These techniques enable the extraction of valuable information directly from raw data, without the need for intermediate image enhancement techniques.

The recent free data availability of the remote sensing multispectral Advanced Spaceborne Thermal Emission and Reflection Radiometer (ASTER); NASA 2001 offer geologists a potentially cost-effective alternative to expensive and time-consuming regional mineral exploration. Recent studies indicate that ASTER data can be used successfully to map the distinct hydrothermal alteration zones of porphyry ore deposits, Pour and Hashim [5], and Alimohammadi et al. [6], especially in arid to semi-arid regions (e.g., Egypt).

However, despite their importance, porphyry deposits are relatively rare in the Precambrian as a result of the poor preservation of upper crustal rocks in tectonically active environments or unfavorable tectonomagmatic conditions that prevent their formation. These conditions are discussed in more detail in previous works, such as ([7] and [8]).

Porphyry deposits are the world’s most important source of Cu and Mo and are major sources of Au, Ag, and Sn. They account for about 50%–60% of world Cu production and more than 95% of world Mo production [9]. Porphyry deposits are large, low- to medium-grade deposits that are spatially and genetically related to felsic intermediate porphyritic intrusions. The deposits are characterized by distinctive and widespread hydrothermal alteration zones, which provide a useful footprint for exploration [9], [10], [11]. Because porphyry deposits generally form in the upper crust, at less than 5–10 km paleodepths, in tectonically unstable convergent plate margins and are prone to erosion, more than 90% of known deposits are Cenozoic or Mesozoic in age.

The Arabian Nubian Shield (ANS), which extends from Egypt in the west to Saudi Arabia and Oman in the east and

Manuscript received 12 July 2023; revised 8 September 2023; accepted 29 September 2023. Date of publication 3 October 2023; date of current version 13 October 2023. (Corresponding author: Mohammed M. Abdelsamea.)

Usama Zidan and Mohamed Medhat Gaber are with the School of Computing and Digital Technology, Birmingham City University, B5 5JU Birmingham, U.K. (e-mail: usama.zidan@bcu.ac.uk; mohamed.gaber@bcu.ac.uk).

Hamdy A. El Desouky is with the Petroleum & Mining Geology, Galala University, Suez Governorate 435611, Egypt, and also with the Geology Department, Menoufia University, Menoufia 6131567, Egypt (e-mail: geohamdy@yahoo.com).

Mohammed M. Abdelsamea is with the School of Computing and Digital Technology, Birmingham City University, B5 5JU Birmingham, U.K., and also with the Department of Computer Science, Faculty of Computers and Information, Assiut University, Assiut 55PG+V6H, Egypt (e-mail: mohammed.abdelsamea@alumni.imtlucca.it).

Digital Object Identifier 10.1109/JSTARS.2023.3321714

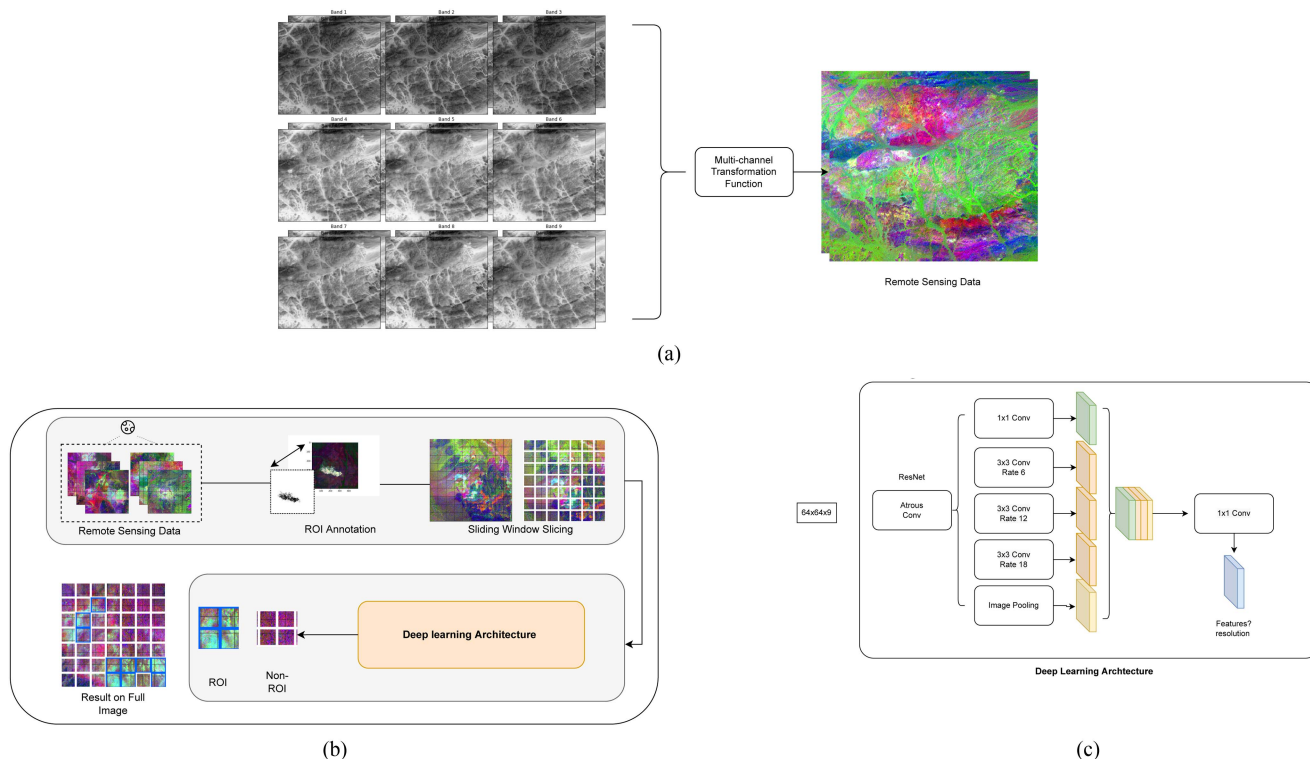


Fig. 1. Image analysis workflow for satellite imagery and mineral detection using CNN. The workflow consists of four steps: (a) acquisition of satellite images of a target area—Multichannel transformation of RAW satellite image, (b) training pipeline begins with annotation of ROI and tiling of the images into smaller segments for feature extraction, and (c) classification of each tile based on its mineral content using a CNN encoder—CNN model architecture. The figure also illustrates some examples of the output of each step, such as a satellite image with ROI annotations and tiles with different colors indicating the presence or absence of mineral deposits.

from Jordan in the north to Eritrea and Ethiopia in the south, constitutes Earth's largest tract of juvenile Neoproterozoic crust. The ANS has an apparent lack of porphyry Cu–Au deposits, Ahmed and Gharib [12], Khalifa et al. [13], and Abd El-Rahman et al. [14], compared with its abundant orogenic gold deposits, which have been mined in Egypt for over 7000 years [15], [16]. This lack is related either to preservation problems during tectonics or to the lack of relevant exploration programs in the vast terrains of the ANS.

Recent advances in remote sensing technology and ML techniques have created new opportunities to explore porphyry copper deposits. High-resolution satellite imagery, when coupled with ML algorithms, can efficiently and accurately identify hydrothermal alteration zones that are associated with these deposits. This technological advancement has the potential to revolutionize the exploration of porphyry copper deposits, especially in areas where they are scarce. By automating image interpretation and reducing the time and cost associated with traditional methods, ML techniques, specifically deep learning, can improve the identification and mapping of hydrothermal alteration zones associated with porphyry copper deposits. Deep learning uses neural networks to learn from large datasets, recognize patterns and features in new data and has been successfully applied in various remote sensing applications, including mineral exploration [17], [18], [19], [20].

In this study, ASTER satellite imagery and image processing techniques were applied to identify hydrothermal alterations

associated with porphyry generalization, see Fig. 1. An image with a unified spatial resolution was developed while maintaining the ASTER spectral details. Our deep learning pipeline assesses images from different regions with the goal of detecting hydrothermal alterations. We utilize a convolutional neural network (CNN) for the analysis of the multispectral images. To mitigate the high computational requirements of the high-resolution images, we employ a patch-based approach using an overlapping window to split the images into tiled fixed-size patches. Data cubes were classified to provide “tile spectra” for locating similar tiles. We utilize hand-labeled patches to classify the image and identify areas of hydrothermal alteration. Our results show that deep learning CNNs are able to successfully identify hydrothermal alterations with high accuracy. Based on this, this article presents several noteworthy contributions given below.

- 1) We devise an effective geographic sampling strategy leveraging multispectral imagery from 20 globally diverse regions. A rigorous Leave-One-Out protocol is used whereby representations are blended and geographic invariant patterns fundamental for generalization.
- 2) We outline an adaptable workflow curating relevant spectral bands, annotating targets, and tuning architectures to blueprint deep learning pipelines for mineral exploration.
- 3) We evaluate across globally dispersed study areas to demonstrate the methodology's robustness and adaptability in consistently achieving high-accuracy alteration fingerprinting.

The high level of spectral resolution and spatial detail offered by the ASTER data proves to be invaluable to understanding patterns related to important elements found within mineral deposits. In addition, it aids in detecting geological structures and variations in lithology that are instrumental in deposit formation. By accurately delineating areas exhibiting hydrothermal alterations, ASTER imagery assists in identifying potential regions worthy of further investigation for precious or base metals. Our research holds promising potential for advancing precise mineral exploration techniques through the integration of advanced artificial intelligence methodologies with ASTER imagery.

The rest of this article is organized as follows. In Section II, we review some recent techniques and applications of deep learning in remote sensing. Section III describes the methodology of our approach, including the different pre-processing producers used, CNN architecture details, and training hyperparameters. Section IV presents the experimental results of our experiments with a discussion demonstrating the applicability of the proposed method to the dataset. Finally, Section V concludes this article.

II. BACKGROUND

Remote sensing has become an increasingly essential technique for mineral exploration due to its ability to provide a cost-effective means of obtaining large-scale and high-resolution data [21], [22]. However, there are significant hurdles to processing and analyzing remote sensing data, including high dimensionality, noise, and data variability [23], [24].

ML has evolved as a useful technique for remote sensing data interpretation in response to these issues. ML approaches can manage large-scale and complicated datasets by automatically extracting useful features from raw data [25], [26], [27], [28]. Numerous studies have examined the use of ML for mineral exploration utilizing remote sensing data. In particular, the use of ML for mineral exploration has been extensively reviewed in recent years. For example, Signoroni et al. [29], provided a comprehensive review of various ML algorithms and their applications in remote sensing data analysis for mineral exploration. They highlighted the effectiveness of decision trees, random forests, and support vector machines in mineral exploration tasks. Similarly, recent trends in image processing gearing toward deep learning techniques in mineral exploration using remote sensing data. One of the common approaches for multispectral image classification is to use 3-D CNNs that can capture both spatial and spectral features from the input images. Navarro et al. [30] proposed an ad hoc architecture called 3DeepM that consists of 3-D filter banks specially designed to extract spatial spectral features in multichannel images. The authors applied their method to several aerial and satellite image datasets and achieved competitive results. However, one of the drawbacks of this approach is that it requires a large amount of training data and computational resources to optimize the 3-D filters. Wu et al. [31] proposed a cross-channel reconstruction (CCR) module that enables compact fused representations by reconstructing and exchanging information across modalities, such as hyperspectral, LiDAR, and SAR data. The model,

CCR-Net, demonstrates improved classification over existing multimodal fusion techniques on two datasets. The modular CCR design allows integration with different CNN backbones in an end-to-end fashion. This showcases the benefits of explicitly modeling intermodality relationships versus simple feature concatenation. Their work highlights the potential for cross-modal reconstruction and information exchange to learn joint representations from heterogeneous remote sensing data. Another approach is to use multiview learning techniques that can exploit different representations or modalities of the same data. For example, Pande and Banerjee [32] proposed a deep multiview learning framework for hyperspectral image classification that combines spectral features extracted by a 1-D CNN with spatial features extracted by a 2-D CNN. The spectral–spatial attention module uses 1-D and 2-D CNNs to learn spectral and spatial attention masks that highlight the discriminative features of the hyperspectral images. The attention masks are then adaptively combined using an adaptive learning mechanism that learns the optimal weights for each mask. The combined attention features are then fed to a 3-D CNN classifier that performs the final classification.

Hong et al. [33] proposed a multimodal deep learning framework for remote sensing image classification. They aim to address three key challenges—what to fuse, how to fuse, and where to fuse across modalities, such as SAR, multispectral, and hyperspectral data. Five different fusion modules are introduced and evaluated, including early, middle, and late fusion strategies in addition to encoder–decoder and cross-fusion architectures. The modules are integrated in a flexible framework allowing pixelwise classification with fully connected networks and spatial–spectral classification with CNNs. Experiments on three distinct multimodal datasets demonstrate improved accuracy over single modal baselines. The cross-fusion approach appears most effective by enabling compact joint representations. However, the fusion techniques evaluated remain relatively simplistic. More complex relationships between modalities could be exploited.

A third approach is to use attention-guided methods that can focus on the most relevant regions or features of the input images. For example, Liu et al. [34] proposed an attention-guided multispectral and panchromatic image classification method that uses a dual-branch network with two attention modules: one to select informative regions from panchromatic images and second to improve discriminative features from multispectral images. The authors evaluated their method on three datasets of remote sensing images and achieved superior performance over the existing methods. However, this approach may not be able to capture intraband features that are important for distinguishing different types of minerals and alterations.

Some recent work [35] demonstrates the potential of graph convolutional networks (GCNs) to supplement CNNs for spectral image analysis. Specifically, this article explores the combination of CNNs and GCNs for hyperspectral image classification. They propose a mini-batch GCN architecture to reduce the computational cost of traditional GCNs for large-scale data. Their approach also enables out-of-sample inference without retraining. By comparing CNNs and GCNs, they demonstrate that GCNs can complement CNNs by modeling spatial relationships.

TABLE I
SUMMARY OF THE DATASET COMPRISING THE REGIONS EMPLOYED FOR TRAINING AND TESTING

Region	Number of study areas	References
Sudan	1	[39], [40], [41]
Namibia	1	[42], [43], [44]
Argentina	4	[45], [46], [47], [48], [49], [50], [51], [52], [53], [54], [55], [56]
Iran	4	[57], [58], [59], [60], [61], [62], [63], [64], [65], [66], [67], [68], [69], [70]
Pakistan	3	[71], [72], [73], [74], [75], [76], [77],
USA	5	[71], [78], [79], [80], [81], [82], [83] [84], [85], [86], [87], [88], [89]
China	Test area 1	[90], [91], [92]
China	Test area 2	[93], [94], [95]

Each study area is represented by a minimum of one ASTER image, accompanied by references to the relevant literature affirming the presence of porphyry deposits within these regions.

While several studies have examined the use of ML approaches for multispectral image classification in remote sensing data, only a few have attempted to apply deep learning techniques to the specific goal of porphyry deposit classification. This is a particularly difficult endeavor since porphyry deposits frequently represent a small fraction of the available data and are difficult to identify from surrounding rocks due to their low contrast and weak spectral characteristics [36]. Recent studies have proposed alternative deep learning algorithms for porphyry deposit categorization utilizing remote sensing data to overcome these problems, which will be addressed in this article.

Fu et al. [37] applied a CNN model for mineral prospectivity mapping of porphyry copper deposits using remote sensing imagery and geochemical data in the Duolong ore district in Tibet. The CNN model achieved a high accuracy of 0.956 and identified several potential exploration targets. The study compared the CNN model with conventional ML models, highlighting the effectiveness of deep learning techniques for porphyry deposit classification. However, the study did not consider the influence of topography and geological structures on mineral prospectivity mapping, which could be further explored in future studies.

Zhang and Cheng [38] proposed a deep learning method based on a stacked autoencoder (SAE) and a Softmax regression classifier for mineral prospectivity mapping in the Yawan-Daqiao porphyry copper belt in Tibet. The SAE model achieved an accuracy of 0.94 and outperformed other ML models, such as the support vector machine, random forest, and logistic regression. The study demonstrated the potential of deep learning techniques for the classification of porphyry deposits. However, the study did not consider the spectral variability of different porphyry deposits and the effects of mixed pixels, which could be further explored in future studies.

Overall, these studies demonstrate the potential of deep learning techniques for porphyry deposit classification and mineral prospectivity mapping using remote sensing data. However, there are still gaps in understanding the influence of geological structures and topography on mineral prospectivity mapping, spectral variability of different porphyry deposits, and the effects of atmospheric correction and noise reduction. Further research is needed to address these gaps and advance the application of deep learning techniques for mineral exploration.

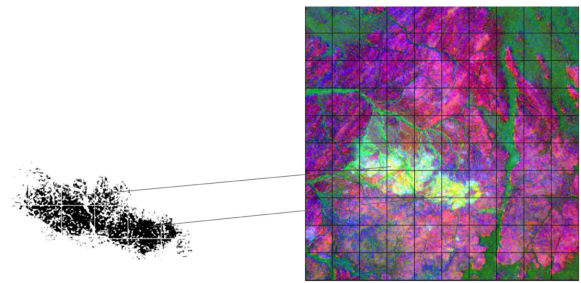


Fig. 2. Example annotation mask.

III. METHODOLOGY

A. Dataset

The study was conducted in 20 porphyry deposits in seven regions. Table I gives a distribution of the 20 study areas chosen with their references in the literature. Images were derived from the ASTER Satellite. ASTER data are typically composed of 14 spectral bands with different spatial and spectral resolutions. In total, three bands in the visible near-infrared (VNIR) spectrum with 15 m spatial resolution, six bands in the shortwave infrared (SWIR) with 30 m spatial resolution, and five bands in the thermal infrared spectrum with 90 m spatial resolution. Cloud-free scenes of ASTER Level 2 Surface Reflectance VNIR and SWIR V003 (AST07) covering the study areas were obtained from NASA [96]. The scenes were acquired daytime and pregeoreferenced to the UTM projection using the WGS-84 datum. Radiometric, geometric, and atmospheric corrections were applied to the image data. The SWIR data were further corrected for crosstalk and parallax errors due to the spatial locations of SWIR bands. Spectral resampling has been used to downscale the spatial resolution of the six SWIR ASTER bands to 15 m resolution, then, the data have been resized to study areas.

Fig. 2 shows the image annotations used for training our deep learning model were obtained through objective manual marking of the preprocessed ASTER satellite imagery. Objective manual marking involves the systematic identification and delineation of specific regions that have been previously recognized as hosting porphyry deposits in earlier research. Specifically, the raw multispectral ASTER images were preprocessed using

techniques including band ratios (BRs) and mathematical-based band blending to highlight regions with spectral signatures indicative of alteration minerals. We then carefully examined these preprocessed images to identify and delineate areas exhibiting these alteration patterns. Appropriate masks were manually created to annotate these regions of interest (ROIs) based on the visual interpretation. Since the annotations were guided by both the preprocessed outputs and expert knowledge, this facilitated accurate labeling of the alteration zones critical for training the deep neural network. The manually created masks were then used to extract labeled patches from the raw multispectral bands during the training phase. Using expert annotations tailored to geology and remote sensing characteristics, our model could effectively learn the desired spectral–spatial features associated with hydrothermal alterations and porphyry deposits. The customized training process led to high accuracy in detecting minerals indicative of porphyry-type ore deposits across diverse and unseen geographic areas.

B. Image Processing

Traditional remote sensing analyses were performed to fingerprint hydrothermal alterations in different areas. Several image-processing techniques, including principal component analysis (PCA), minimum noise fraction (MNF), BRs, and band math (BM) were applied based on spectral characteristics of alteration key minerals for a systematic selective extraction of hydrothermal alteration zones. The processed images were displayed in RGB color channels to generate false color composites highlighting hydrothermal alterations for deep learning annotation. PCA is a multivariate statistical technique that selects uncorrelated linear combinations (eigenvector loadings) of variables in such a way that each component successively extracted linear combination and has a smaller variance. A standard PCA transformation was applied to the VNIR and SWIR ASTER data. The MNF transformation is used to determine the inherent dimensionality of image data, segregate noise in the data, and reduce the computational requirements for subsequent processing [97]. A standard MNF transformation was applied to the VNIR and SWIR ASTER data. BRs are a technique where the DN value of one band is divided by the DN value of another band. BRs are useful for highlighting certain features or materials that cannot be seen in the raw bands (e.g., [98]). A wide range of BRs was performed in the ASTER data. BM is a technique, which allows inserting the DN values of bands in mathematical formulas [99]. The performed indices include the OH-bearing altered minerals index ($OHI = 7/6 \times 4/6$), the kaolinite index ($KLI = 4/5 \times 8/6$), the alunite index ($ALI = 7/5 \times 7/8$), and the calcite index ($CLI = 6/8 \times 9/8$).

C. Deep Learning

Deep learning, a branch of ML, is concerned with developing complex neural network architectures that emphasize a large number of layers. A key feature that allows these models to interpret complex data structures and types. In our work, we utilized a deep neural network to process the multispectral images and learn a probability distribution of the target classes.

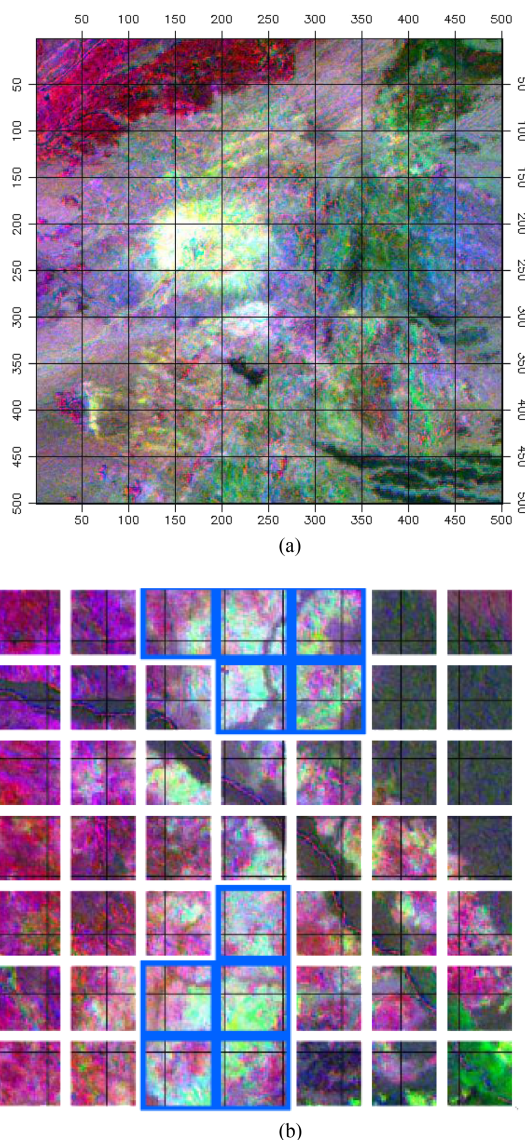


Fig. 3. Example processed region. (a) Sample training region. (b) Sample prediction of model perpatch, ROI highlighted in blue.

Our model processes the temporal effects captured in the image bands in order to extract both spatial and intraband features.

The data used in this article consist of 18 multispectral training images that were manually sourced from ASTER, as mentioned in Section III-B. The raw ASTER images have nine channels and a resolution of 500×500 pixels. Using the processed RGB images, we were able to identify the hydrothermal alteration zones as ROIs, which were then masked and saved to be used in the tiling processing stage. We also applied data augmentation techniques, such as random rotation, flipping, and scaling to increase the diversity and robustness of the data. Using an overlapping window, the image was tiled into a fixed-size grid. The grid size was chosen to correspond to the dimensions of the provided image. Fig. 3 illustrates a tiled image and model predictions. The extraction of overlapping patches allows the construction of large patch databases. These patches are what the neural network uses for inference later in the testing step. The

tiling process involves dividing the large images into smaller, more manageable tiles, which can be processed individually using our deep learning pipeline.

With overlapping training patches, models are exposed to more varied imagery content within spatial neighborhoods covered by multiple tiles. These additional examples can help us learn local textural cues and subtle spectral variations associated with hydrothermal zones. It also provides denser sampling that may better encapsulate spatial relationships and alteration boundaries. Furthermore, data augmentation techniques, such as random cropping, flipping, and rotation during training can further increase variability from the overlapped areas.

Our innovative approach allows for the exploration of porphyry ore deposits in remote areas while reducing reliance on expensive and time-consuming ground surveys. Consequently, it presents novel opportunities to uncover previously unidentified porphyry occurrences. In addition, by harnessing advanced deep learning models, we can discern intricate spectral–spatial patterns within multispectral data that may be challenging for human observers to perceive. As a result, more accurate predictions regarding the potential presence of porphyry deposits can be made. The significance of this advancement extends beyond academia as it facilitates efficient and sustainable resource exploration. With increasing mineral demand coupled with the need for responsible resource utilization, developing state-of-the-art technologies that enable effective and precise mineral prospecting strategies becomes imperative. We demonstrate the adaptation of DeepLabv3+, a deep CNN architecture, to accurately fingerprint hydrothermal alterations in ASTER multispectral imagery. Our methodology exploits DeepLabv3+'s capabilities for end-to-end learning to extract spectral–spatial representations tailored to alterations. Through rigorous data curation, training, and testing, we showcase high-accuracy detection across diverse regions.

Specifically, our approach involves adapting the DeepLabv3+ architecture with its core components of atrous convolutional layers, pooling layers, and fully connected layers for this novel application. Atrous convolutions, also known as dilated convolutions, are a variant of traditional convolutional layers that allow expanding the receptive field without increasing parameters. By inserting zeros between input pixels and convolutional kernel weights, the field of view can be efficiently expanded to incorporate larger spatial context. At each layer, the input image is convolved with a set of K kernels and additional biases, resulting in the generation of a new feature map. These features undergo an elementwise nonlinear transformation, and the same process is repeated for each convolutional layer. Unlike multi-layer perceptrons, which aggregate the values of pixels within a neighborhood of a specified size using a permutation-invariant function, such as max or mean operation, CNNs aggregate the values of pixels using convolution operations. Finally, fully connected layers, which are typical neural network layers, are added after the conclusion of the convolutional layers to arrive at the network's prediction.

In particular, we apply DeepLabv3+ to annotated ROIs derived from the raw ASTER multispectral bands. The model is trained on a subset of image patches extracted in a tiled fashion

to enable localized feature learning. Training involves multiple epochs to allow the convolutional kernels to adjust and capture relevant spectral–spatial patterns related to hydrothermal alterations. Once trained, the model can accurately classify each patch and delineate the full spatial extent of alterations when applied across the entire image.

The curated dataset of patches is separated into two classes, namely ROIs with hydrothermal alterations and background regions. Since the patches are sourced from 20 different regions, training and testing were done using a Keep-One-Out strategy. Furthermore, patches from 18 regions are used to train the network parameters, leaving testing to be done on the remaining regions' patches. To evaluate the model's generalization ability, we adopt the Keep-One-Out approach, where we leave out one region from the training set and use it for testing. Specifically, during training, we use patches from all but one of the regions to train the model. Then, the model is tested on the patches from the remaining region that were not included in the training set.

This approach simulates a scenario where the model is tested on regions that it has never seen before. By leaving one region out during training, the model is forced to learn features that are not specific to a particular region and are more generalizable. The model must learn to recognize hydrothermal alteration zones based on the patterns and features present in the input image, rather than simply memorizing features unique to a particular region. Adapting deep neural networks, such as DeepLabv3+ to multispectral mineral detection necessitates analyzing high-resolution imagery, imposing nontrivial computational requirements. However, through model optimization we demonstrate efficient learning for this novel application. Specifically, DeepLabv3+ significantly reduces complexity versus other architectures via four main optimizations—fewer parameters owing to its light encoder–decoder structure, which lowers memory and operations, patch-based training focusing learning on cropped regions rather than full images reducing GPU burden, single-scale processing avoiding creating multiple image versions, and atrous convolutions expanding the receptive field without increasing parameters compared with standard kernels, efficiently incorporating larger spatial context. Together, these optimizations enable high-accuracy mineral detection using DeepLabv3+ with a single commercial GPU. Further improvements in model compression and quantization can potentially yield additional efficiency gains, opening new possibilities for operational deployment.

By using the Keep-One-Out strategy, we can assess the performance of the model on unseen regions and evaluate its generalization ability. This approach is particularly useful in geological mapping applications, where the model's ability to generalize to new regions is crucial. The model learns a probability distribution over the target classes. The last two nodes of the network output a probability that estimates whether a given input belongs to the corresponding class. The final accuracy metrics are calculated using the maximum probability. Over the learning process, the convolutional kernel parameters constantly adjust to filter out noisy signals from the nine channels. Once the model converges, we arrive at a parameter set that is able to isolate a fingerprint identifying the hydrothermal alterations.

IV. RESULTS AND DISCUSSIONS

Our deep learning approach was used to identify hydrothermal alteration zones in ASTER multispectral images. The utilization of ASTER imagery has become an integral tool in the field of mineral exploration. It plays a crucial role in identifying and mapping minerals, as well as capturing alteration zones on the Earth’s surface. The high level of spectral resolution and spatial detail offered by ASTER data proves to be invaluable for understanding patterns related to important elements found within mineral deposits. In addition, it aids in detecting geological structures and variations in lithology that are instrumental in deposit formation. By accurately delineating areas exhibiting hydrothermal alterations, ASTER imagery assists in identifying potential regions worthy of further investigation for precious or base metals. Our research holds promising potential for advancing precise mineral exploration techniques through the integration of advanced artificial intelligence methodologies with ASTER imagery. Specifically, we delineate that the training corpus consists of 18 (ASTER) images spanning confirmed porphyry deposit locations globally. The 500×500 pixel raw images encompass nine spectral bands with VNIR and SWIR wavelengths sensitive to hydrothermal alteration minerals. Through specialized preprocessing, regions exhibiting alteration signatures are extracted and annotated as ROIs. Using an overlapping windowing approach, a dataset totaling approximately 14000 samples for each alteration ROI and background class is compiled. We employ a rigorous methodology validating the models using fivefold stratified cross-validation during training and report accuracy metrics averaged over the folds.

The model learns a probability distribution over the target classes and outputs a probability estimate of whether a given input belongs to the corresponding class. The convolutional kernel parameters adjust over the learning process to filter out noisy signals from the nine channels. The final accuracy metrics are calculated using the maximum probability, and the model converges to a parameter set that isolates a fingerprint identifying the hydrothermal alterations. Overall, this methodology provides a promising approach for accurately detecting hydrothermal alteration zones in multispectral satellite imagery using deep learning.

We evaluate the performance of the proposed method on several metrics, such as precision, recall, and F1-score. The results show that the method can effectively identify hydrothermal alteration zones in multispectral images with high accuracy and robustness. We also tested its performance in completely unseen regions located in China. This testing aimed to determine the ability of the model to identify hydrothermal alteration zones in patches that were not sourced from the same or nearby regions. The results showed that the model was able to maintain high accuracy and robustness, indicating its strong potential for application in various geological contexts.

The results of the region classification task show promising results, with some regions performing better than others. The classification models performed well in predicting the regions of Iran 2, Pakistan 1, and USA 6, achieving recall scores of 1.0.

TABLE II
TEST SCORES FOR PRECISION, RECALL, AND F1-SCORE IN IDENTIFYING HYDROTHERMAL ALTERATION ZONES IN MULTISPECTRAL IMAGES ACROSS DIFFERENT REGIONS

Area	Recall	Precision	F1-score
Argentina 1	1.0	0.287	0.446
Argentina 2	0.654	0.542	0.583
Argentina 3	0.917	0.351	0.5
Argentina 4	0.857	0.55	0.669
Iran 1	0.125	1.0	0.222
Iran 2	1.0	0.622	0.752
Iran 3	0.75	1.0	0.857
Iran 4	0.6	0.875	0.64
Iran 3	0.667	0.649	0.581
Iran 4	1.0	0.438	0.606
Namibia 1	0.833	0.633	0.708
Pakistan 1	0.714	0.217	0.333
Pakistan 2	0.429	0.18	0.238
Pakistan 3	0.5	0.6	0.476
Sudan 1	0.333	1.0	0.5
USA 1	0.333	0.167	0.222
USA 2	0.8	0.647	0.602
USA 4	0.75	1.0	0.833
China 1	0.125	0.273	0.167
China 2	0.667	0.727	0.696

Results indicate high accuracy and robustness of the proposed method. Notably, the models trained on all regions except China were tested on completely “unseen” regions, demonstrating their generalizability. The F1-scores ranged from 0.22 to 0.83, with the highest scores achieved in Namibia 1 and USA 4 regions.

However, there were some regions where the models performed poorly, such as Sudan 1 and Argentina 1, with recall scores of 0.43 and 0.10, respectively.

Table II gives the results of the testing phase in our experiments. Since one region was left out in each run, we test our model on unseen patches to be able to gauge the generalizable aspect of the model performance. We observed that the recall varied across regions, indicating that some regions were easier to detect than others. For example in Fig. 4, Argentina regions had the highest recall, which could be explained by the fact that they always had some patches from the same region in the training set. Similarly, Iran regions performed well, as two of them were among the top 10 in the recall. These results suggest that some regions share common features or patterns in their “tile-spectra” that help the model to recognize them better. On the other hand, some regions had a low recall, implying that they lacked distinctive or representative features that could be learned from other regions. For instance, (USA 4) had a poor recall despite having patches from other USA regions (1–6) and other countries in the training set. These results demonstrate the importance of including a variety of regions in the training set to improve the accuracy and generalizability of the model. The results of the regionwise evaluation are presented in Table II. The evaluation metrics used in this study are recall, precision, and F1-score. Recall measures the proportion of relevant patches correctly identified by the model, whereas precision assesses the

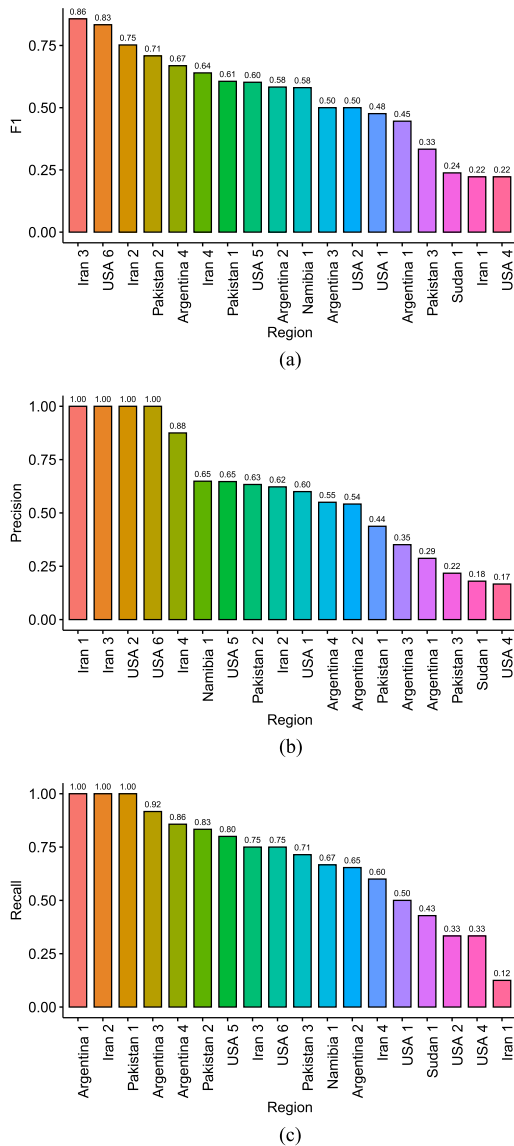


Fig. 4. Quantitative results on perregion testing. (a) F1-Score. (b) Precision. (c) Recall.

proportion of patches detected by the model that are truly relevant. The F1-score provides a balanced measure of the model's overall performance by considering both recall and precision. The model evaluation results for various regions reveal varying levels of performance. Argentina 1 exhibited excellent recall but low precision, whereas Argentina 2 got a good F1-score but recognized a lot of irrelevant patches. Argentina 3 had a high recall but a low precision, and Argentina 4 had a high recall but a low precision.

In Iran 1, the model had a high precision but a low recall. Iran 2 had a recall but poor precision, whereas Iran 3 had excellent precision but poor recall. Iran 4 has relatively high precision, however, the model omitted numerous important regions.

Areas in the Pakistan region exhibited a higher recall than precision, demonstrating the model's ability to recognize the relevant regions.

Sudan 1 and USA 1 had low recall and precision scores, implying that the model missed both relevant and irrelevant patches. USA 2 had great precision but low recall, whereas America 4 had low recall and precision ratings. USA 5 had excellent precision but poor memory, whereas USA 6 had flawless recall and precision. The variation in recall and precision between different areas and regions can be attributed to the geological characteristics of the porphyry systems being studied. Further research into the porphyry subclasses, as well as their specific geological attributes [9], would provide valuable insights into understanding how they affect recall and precision in different locations.

These results suggest that the performance of the classification models may be influenced by factors, such as the size and complexity of the region, as well as the availability and quality of the data used to train the models. Regions with smaller populations, such as Namibia 1, may also be more difficult to classify accurately due to the limited amount of available data.

The models were also able to generalize well to unseen patches, which is likely due to the fact that the models were trained on a large dataset of images from a variety of regions. The models were able to learn the patterns that are common to all of the regions, and they were able to generalize these patterns to unseen patches. We have analyzed the factors that could contribute to variations in recall and precision in different areas and regions, including the aspects mentioned in this comment. Through our investigation, we have determined that the geological setting of porphyry systems is the primary factor influencing these variations. It is important to note that porphyry systems encompass a broad range of deposits with diverse geological characteristics and metal enrichments. Further research into the porphyry subclasses, as well as their specific geological attributes, would provide valuable insights into understanding how they affect recall and precision in different locations. We have elaborated on this in the article.

To further investigate the generalizability of model parameters on unseen data, we trained the model on all the regions previously discussed and tested its performance on the new regions' patches. Table II gives results on China 1 and China 2 regions. Based on the evaluation metrics provided in the tables, the model's overall performance in detecting hydrothermal alterations from satellite images appears to be promising. Fig. 5 shows recall scores for most regions are in the range of 0.5–0.875, indicating that the model is able to identify between 50% and 87.5% of the actual hydrothermal alterations present in the images. Furthermore, the precision scores are relatively high, ranging from 0.5 to 1, indicating that the model has a low rate of false positives, i.e., it is correctly identifying areas that do contain hydrothermal alterations.

Focusing on China 1, the model's performance appears to be better than the average, with a recall score of 0.75, indicating that the model is detecting 75% of the hydrothermal alterations present in the images. The precision score is also 0.75, indicating that the model has a low false positive rate.

Overall, while the model's performance on China 1 appears to be relatively good, the variability in performance across different

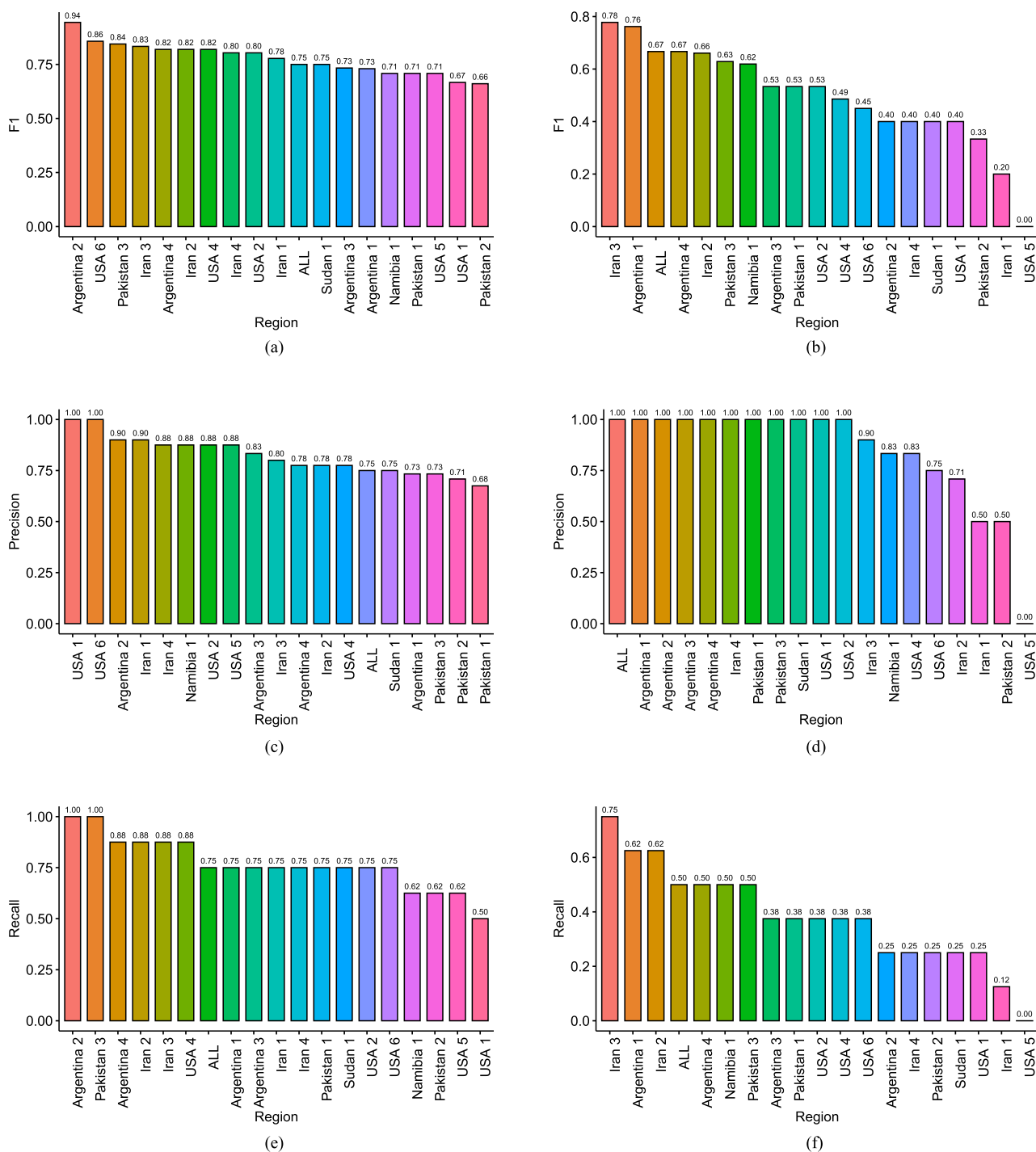


Fig. 5. Quantitative results on China 1 and China 2 regions. (a) F1-Score. (b) F1-Score. (c) Precision. (d) Precision. (e) Recall. (f) Recall.

regions suggests that the model’s accuracy is highly dependent on the characteristics of the specific regions and the images being analyzed. These results suggest that training the model in regions similar to the target region can improve its performance in detecting hydrothermal alterations from multispectral satellite imagery. Therefore, it would be beneficial to incorporate more training data from regions that are similar to the target region to improve the model’s ability to generalize to new regions. Further testing and evaluation on larger and more diverse datasets will

be needed to determine the generalizability and reliability of the model’s performance in detecting hydrothermal alterations from satellite images. Remote sensing data contain inherent variabilities that can impact mineral detection algorithms [100]. However, through our training pipeline we demonstrate that model robustness to these effects can be improved. When multispectral images are obtained from diverse geographic regions worldwide with confirmed deposits, variabilities in illumination, atmospheric noise, and mineral spectra are encapsulated

in the training distribution. Furthermore, data augmentation techniques including random image rotations, flips, and scales during training expose the model to new variations, avoiding overfitting. This improves generalizability as evidenced by our high test accuracy even on completely unseen study areas. While variability remains an open-domain adaptation challenge, our approach shows that deep neural networks can learn robust spectral–spatial features related to hydrothermal alterations despite inherent data noise and artifacts.

V. CONCLUSION

Our study developed a comprehensive workflow and pipeline for fingerprinting porphyry deposits. The pipeline includes a workflow for processing and preprocessing multispectral images to detect patterns of certain minerals based on their spectral reflections.

Future work could explore the extension of our approach to other types of mineral deposits and the incorporation of additional data sources, such as hyperspectral remote sensing data and geophysical data. In general, the results of our study demonstrate the potential of this workflow and pipeline for efficient and accurate identification of porphyry deposits, which are important sources of copper, gold, and molybdenum. Our approach can be used to improve the exploration and mining of these deposits, by providing more precise targeting of exploration efforts and optimizing mining operations.

Future work could extend this approach to other types of deposits and incorporate additional remote sensing data, such as hyperspectral imagery or geophysical data, for improved detection. Evaluating synthetic minority oversampling techniques may also help improve performance on under-represented classes. Extending the approach to additional deposit types, data modalities, and operational scenarios can ultimately enable a more efficient and sustainable discovery of essential ore deposits around the world.

REFERENCES

- [1] C. W. Burnham, "Facies and types of hydrothermal alteration," *Econ. Geol.*, vol. 57, no. 5, pp. 768–784, 1962.
- [2] L. Mathieu, "Quantifying hydrothermal alteration: A review of methods," *Geosciences*, vol. 8, no. 7, pp. 1–27, 2018.
- [3] G. M. Schwartz, "Hydrothermal alteration," *Econ. Geol.*, vol. 54, no. 2, pp. 161–183, 1959.
- [4] W. F. Buckingham and S. E. Sommer, "Mineralogical characterization of rock surfaces formed by hydrothermal alteration and weathering; application to remote sensing," *Econ. Geol.*, vol. 78, no. 4, pp. 664–674, 1983.
- [5] A. B. Pour and M. Hashim, "Application of advanced spaceborne thermal emission and reflection radiometer (ASTER) data in geological mapping," *Int. J. Phys. Sci.*, vol. 6, no. 33, pp. 7657–7668, 2011.
- [6] M. Alimohammadi, S. Alirezaei, and D. J. Kontak, "Application of ASTER data for exploration of porphyry copper deposits: A case study of Daraloo–Sarmeshk area, southern part of the Kerman copper belt, Iran," *Ore Geol. Rev.*, vol. 70, pp. 290–304, 2015.
- [7] J. P. Richards and A. H. Mumin, "Magmatic-hydrothermal processes within an evolving Earth: Iron oxide-copper-gold and porphyry Cu \pm Mo \pm Au deposits," *Geol.*, vol. 41, no. 7, pp. 767–770, 2013.
- [8] B. H. Wilkinson and S. E. Kesler, "Tectonism and exhumation in convergent margin orogens: Insights from ore deposits," *J. Geol.*, vol. 115, no. 6, pp. 611–627, 2007.
- [9] R. H. Sillitoe, "Porphyry copper systems*," *Econ. Geol.*, vol. 105, no. 1, pp. 3–41, 2010. [Online]. Available: <https://doi.org/10.2113/gsecongeo.105.1.3>
- [10] D. R. Cooke, P. Hollings, and J. L. Walshe, "Giant porphyry deposits: Characteristics, distribution, and tectonic controls," *Econ. Geol.*, vol. 100, no. 5, pp. 801–818, 08 2005. [Online]. Available: <https://doi.org/10.2113/gsecongeo.100.5.801>
- [11] J. J. Wilkinson, "Triggers for the formation of porphyry ore deposits in magmatic arcs," *Nature Geosci.*, vol. 6, no. 11, pp. 917–925, 2013.
- [12] A. H. Ahmed and M. E. Gharib, "Porphyry Cu mineralization in the Eastern Desert of Egypt: Inference from geochemistry, alteration zones, and ore mineralogy," *Arabian J. Geosciences*, vol. 9, pp. 1–26, 2016.
- [13] I. H. Khalifa, A. M. Hegazi, and M. Faisal, "Geological setting for porphyry copper deposits in calc-alkaline rocks: Wadi Rofaiyed area, Sinai, Egypt," *Arabian J. Geosciences*, vol. 9, pp. 1–22, 2016.
- [14] Y. Abd El-Rahman, T. Seifert, and A. Said, "The South Um Mongul Cu-Mo-Au prospect in the northern Eastern Desert of Egypt: Tonian porphyry-style mineralization with an Ediacaran hydrothermal iron oxide overprint," *Ore Geol. Rev.*, vol. 99, pp. 217–234, 2018.
- [15] N. Botros, "Gold in Egypt: Does the future get worse or better," *Ore Geol. Rev.*, vol. 67, pp. 189–207, 2015.
- [16] R. Klemm and D. Klemm, *Gold and Gold Mining in Ancient Egypt and Nubia: Geoarchaeology of the Ancient Gold Mining Sites in the Egyptian and Sudanese Eastern Deserts*. Berlin, Germany: Springer, 2012.
- [17] Y. Chen, X. Zhao, and X. Jia, "Spectral–spatial classification of hyperspectral data based on deep belief network," *IEEE J. Sel. Topics Appl. Earth Observ. Remote Sens.*, vol. 8, no. 6, pp. 2381–2392, Jun. 2015.
- [18] Y. Chen, Z. Lin, X. Zhao, G. Wang, and Y. Gu, "Deep learning-based classification of hyperspectral data," *IEEE J. Sel. Topics Appl. Earth Observ. Remote Sens.*, vol. 7, no. 6, pp. 2094–2107, Jun. 2014.
- [19] A. Romero, C. Gatta, and G. Camps-Valls, "Unsupervised deep feature extraction for remote sensing image classification," *IEEE Trans. Geosci. Remote Sens.*, vol. 54, no. 3, pp. 1349–1362, Mar. 2015.
- [20] A. Sharma, X. Liu, X. Yang, and D. Shi, "A patch-based convolutional neural network for remote sensing image classification," *Neural Netw.*, vol. 95, pp. 19–28, 2017.
- [21] S. Ousmanou, E. M. Fozing, M. Kwékam, Y. Fodoue, and L. D. A. Jeatsa, "Application of remote sensing techniques in lithological and mineral exploration: Discrimination of granitoids bearing iron and corundum deposits in southeastern Banyo, Adamawa region- Cameroon," *Earth Sci. Inform.*, vol. 16, no. 1, pp. 259–285, 2023.
- [22] A. A. Aali et al., "Fusion of remote sensing, magnetometric, and geological data to identify polymetallic mineral potential zones in Chakchak region, Yazd, Iran," *Remote. Sens.*, vol. 14, no. 23, 2022, Art. no. 6018.
- [23] T. Caputo, A. Mormone, E. Marino, G. Balassone, and M. Piochi, "Remote sensing and mineralogical analyses: A first application to the highly active hydrothermal discharge area of Pisciarelli in the Campi Flegrei volcanic field (Italy)," *Remote. Sens.*, vol. 14, no. 15, 2022, Art. no. 3526.
- [24] A. B. Pour, B. Zoheir, B. Pradhan, and M. Hashim, "Editorial for the special issue: Multispectral and hyperspectral remote sensing data for mineral exploration and environmental monitoring of mined areas," *Remote. Sens.*, vol. 13, no. 3, pp. 1–418, 2021.
- [25] H. Shirmard, E. Farahbakhsh, R. D. Müller, and R. Chandra, "A review of machine learning in processing remote sensing data for mineral exploration," *CoRR*, vol. 268, 2021, Art. no. 112750.
- [26] K. R. Schulz Hänsch and U. Sörgel, "Machine learning methods for remote sensing applications: An overview," *Proc. SPIE*, vol. 10790, 2018, Art. no. 1079002.
- [27] A. Singh, K. Gaurav, G. K. Sonkar, and C. Lee, "Strategies to measure soil moisture using traditional methods, automated sensors, remote sensing, and machine learning techniques: Review, bibliometric analysis, applications, research findings, and future directions," *IEEE Access*, vol. 11, pp. 13605–13635, 2023.
- [28] X. Wu, D. Hong, and J. Chanussot, "UIU-Net: U-Net in U-Net for infrared small object detection," *IEEE Trans. Image Process.*, vol. 32, pp. 364–376, Dec. 15, 2022.
- [29] A. Signoroni, M. Savardi, A. Baronio, and S. Benini, "Deep learning meets hyperspectral image analysis: A multidisciplinary review," *J. Imag.*, vol. 5, no. 5, pp. 1–32, 2019.
- [30] P. J. Navarro, L. R. Miller, A. Gila-Navarro, M. V. Díaz-Galián, D. J. Aguila, and M. Egea-Cortines, "3DeepM: An ad hoc architecture based on deep learning methods for multispectral image classification," *Remote. Sens.*, vol. 13, no. 4, pp. 1–22, 2021.

- [31] X. Wu, D. Hong, and J. Chanussot, "Convolutional neural networks for multimodal remote sensing data classification," *IEEE Trans. Geosci. Remote Sens.*, vol. 60, Nov. 2, 2021, Art. no. 5517010.
- [32] S. Pande and B. Banerjee, "Adaptive hybrid attention network for hyperspectral image classification," *Pattern Recognit. Lett.*, vol. 144, pp. 6–12, 2021.
- [33] D. Hong et al., "More diverse means better: Multimodal deep learning meets remote-sensing imagery classification," *IEEE Trans. Geosci. Remote Sens.*, vol. 59, no. 5, pp. 4340–4354, May 2021.
- [34] B. Liu, A. Yu, X. Yu, R. Wang, K. Gao, and W. Guo, "Deep multiview learning for hyperspectral image classification," *IEEE Trans. Geosci. Remote Sens.*, vol. 59, no. 9, pp. 7758–7772, Sep. 2021.
- [35] D. Hong, L. Gao, J. Yao, B. Zhang, A. Plaza, and J. Chanussot, "Graph convolutional networks for hyperspectral image classification," *IEEE Trans. Geosci. Remote Sens.*, vol. 59, no. 7, pp. 5966–5978, Jul. 2020.
- [36] L. C. Neal, J. J. Wilkinson, P. J. Mason, and Z. Chang, "Spectral characteristics of propylitic alteration minerals as a vectoring tool for porphyry copper deposits," *J. Geochemical Exploration*, vol. 184, pp. 179–198, 2018.
- [37] Y. Fu, Q. Cheng, L. Jing, B. Ye, and H. Fu, "Mineral prospectivity mapping of porphyry copper deposits based on remote sensing imagery and geochemical data in the Duolong ore district, Tibet," *Remote Sens.*, vol. 15, no. 2, pp. 1–24, 2023.
- [38] L. Zhang and B. Cheng, "A stacked autoencoders-based adaptive subspace model for hyperspectral anomaly detection," *Infrared Phys. Technol.*, vol. 96, pp. 52–60, 2019.
- [39] F. Bierlein et al., "Petrogenesis of a Neoproterozoic magmatic arc hosting porphyry Cu-Au mineralization at Jebel Ohier in the Gebelt Terrane, NE Sudan," *Ore Geol. Rev.*, vol. 79, pp. 133–154, 2016.
- [40] F. P. Bierlein et al., "New insights into the evolution and age of the Neoproterozoic Jebel Ohier porphyry copper deposit, Red Sea Hills, northeastern Sudan," *Econ. Geol.*, vol. 115, no. 1, pp. 1–31, 2020.
- [41] F. Bierlein et al., "The Jebel Ohier deposit—a newly discovered porphyry copper–gold system in the Neoproterozoic Arabian–Nubian shield, Red Sea Hills, NE Sudan," *Mineralium Deposita*, vol. 51, no. 6, pp. 713–724, 2016.
- [42] C. Mielke, C. Rogass, N. Boesche, K. Segl, and U. Altenberger, "En-GeoMap 2.0—automated hyperspectral mineral identification for the German EnMap space mission," *Remote Sens.*, vol. 8, no. 2, pp. 1–26, 2016.
- [43] R. Hewson, E. Chinkaka, M. van der Meijde, B. Baugh, N. Titus, and J. Mubita, "Geological investigations with high spatial resolution WV-3 satellite imagery and regional geophysics at the Haib Cu porphyry, Namibia," *ASEG Extended Abstr.*, vol. 2019, no. 1, pp. 1–5, 2019.
- [44] X. Meng et al., "Oxidized sulfur-rich arc magmas formed porphyry Cu deposits by 1.88 Ga," *Nature Commun.*, vol. 12, no. 1, pp. 1–9, 2021.
- [45] F. J. Testa, C. Villanueva, D. R. Cooke, and L. Zhang, "Lithological and hydrothermal alteration mapping of epithermal, porphyry and tourmaline breccia districts in the Argentine Andes using ASTER imagery," *Remote Sens.*, vol. 10, no. 2, pp. 1–45, 2018.
- [46] G. H. Poole et al., "The petrogenesis of back-arc magmas, constrained by zircon O and Hf isotopes, in the Frontal Cordillera and Precordillera, Argentina," *Contributions to Mineral. Petrol.*, vol. 175, no. 9, pp. 1–21, 2020.
- [47] G. L. Delendatti, "Caracterización de zonas de alteración hidrotermal en las márgenes del río Castaño, provincia de San Juan, mediante procesamiento digital de imágenes TM," *Revista de la Asociación Geológica Argentina*, vol. 58, no. 1, pp. 97–108, 2003.
- [48] L. Maydagán, M. Franchini, D. Lentz, J. Pons, and C. McFarlane, "Sulfide composition and isotopic signature of the Altar Cu-Au deposit, Argentina: Constraints on the evolution of the porphyry–epithermal system," *Can. Mineralogist*, vol. 51, no. 6, pp. 813–840, 2013.
- [49] L. Maydagán, M. Franchini, M. Chiaradia, J. Dilles, and R. Rey, "The Altar porphyry Cu-(Au-Mo) deposit (Argentina): A complex magmatic-hydrothermal system with evidence of recharge processes," *Econ. Geol.*, vol. 109, no. 3, pp. 621–641, 2014.
- [50] C. Zwahlen, S. Cioldi, T. Wagner, R. Rey, and C. Heinrich, "The porphyry Cu-(Mo-Au) deposit at Altar (Argentina): Tracing gold distribution by vein mapping and LA-ICP-MS mineral analysis," *Econ. Geol.*, vol. 109, no. 5, pp. 1341–1358, 2014.
- [51] L. Maydagán et al., "Porphyry to epithermal transition in the Altar Cu-(Au-Mo) deposit, Argentina, studied by cathodoluminescence, LA-ICP-MS, and fluid inclusion analysis," *Econ. Geol.*, vol. 110, no. 4, pp. 889–923, 2015.
- [52] L. Maydagán, M. Franchini, A. Impiccini, and D. Lentz, "Phyllosilicates geochemistry and distribution in the Altar porphyry Cu-(Au) deposit, Andes Cordillera of San Juan, Argentina: Applications in exploration, geothermometry, and geometalurgy," *J. Geochemical Exploration*, vol. 167, pp. 83–109, 2016.
- [53] L. Maydagán et al., "Petrogenesis of Quebrada de la Mina and Altar North porphyries (Cordillera of San Juan, Argentina): Crustal assimilation and metallogenic implications," *Geosci. Front.*, vol. 8, no. 5, pp. 1135–1159, 2017.
- [54] L. Maydagán, M. Zattin, C. Mpodozis, D. Selby, M. Franchini, and L. Dimieri, "Apatite (U–Th)/He thermochronology and Re–Os ages in the Altar region, central Andes (31°30' s), main Cordillera of San Juan, Argentina: Implications of rapid exhumation in the porphyry Cu (Au) metal endowment and regional tectonics," *Mineralium Deposita*, vol. 55, no. 7, pp. 1365–1384, 2020.
- [55] D. Pérez, P. D'Odorico Benites, and M. Godeas, "Reconnaissance of hydrothermal alteration with the ASTER sensor, in the middle course of Río Santa Cruz (31° 40' s), province of San Juan," *Revista de la Asociación Geológica Argentina*, vol. 66, no. 4, pp. 623–633, 2010.
- [56] L. Maydagán et al., "Petrology of the Miocene igneous rocks in the Altar region, main Cordillera of San Juan, Argentina, a geodynamic model within the context of the Andean flat-slab segment and metallogenesis," *J. South Amer. Earth Sci.*, vol. 32, no. 1, pp. 30–48, 2011.
- [57] A. Hezarkhani, "Hydrothermal fluid geochemistry at the Chah-Firuzeh porphyry copper deposit, Iran: Evidence from fluid inclusions," *J. Geochemical Exploration*, vol. 101, no. 3, pp. 254–264, 2009.
- [58] M. Honarmand, H. Ranjbar, and J. Shahabpour, "Combined use of ASTER and ALI data for hydrothermal alteration mapping in the north-western part of the Kerman Magmatic Arc, Iran," *Int. J. Remote Sens.*, vol. 34, no. 6, pp. 2023–2046, 2013.
- [59] S. Alaei Moghadam, M. Karimi, and M. Sadi Mesgari, "Application of a fuzzy inference system to mapping prospectivity for the Chahfiruzeh copper deposit, Kerman, Iran," *J. Spatial Sci.*, vol. 60, no. 2, pp. 233–255, 2015.
- [60] M. Aghazadeh, Z. Hou, Z. Badrzadeh, and L. Zhou, "Temporal–spatial distribution and tectonic setting of porphyry copper deposits in Iran: Constraints from zircon U–Pb and molybdenite Re–Os geochronology," *Ore Geol. Rev.*, vol. 70, pp. 385–406, 2015.
- [61] H. Mohammaddoost et al., "Zircon U–Pb and molybdenite Re–Os geochronology, with S isotopic composition of sulfides from the Chah-Firuzeh porphyry Cu deposit, Kerman Cenozoic Arc, SE Iran," *Ore Geol. Rev.*, vol. 88, pp. 384–399, 2017.
- [62] M. Safari, A. Maghsoudi, and A. B. Pour, "Application of Landsat-8 and ASTER satellite remote sensing data for porphyry copper exploration: A case study from Shahr-e-Babak, Kerman, south of Iran," *Geocarto Int.*, vol. 33, no. 11, pp. 1186–1201, 2018.
- [63] N. Taghipour and H. Mohammadi Laghab, "Sara (Parkam) porphyry copper deposit in Kerman, Iran: Petrography, geochemistry and geodynamic setting," *Geochemistry J.*, vol. 1, no. 3, pp. 14–26, 2014.
- [64] A. Alirezai, M. Arvin, and S. Dargahi, "Adakite-like signature of porphyry granitoid stocks in the Meiduk and Parkam porphyry copper deposits, NE of Shahr-e-Babak, Kerman, Iran: Constraints on geochemistry," *Ore Geol. Rev.*, vol. 88, pp. 370–383, 2017.
- [65] E. Mahmoudi, F. Moore, and S. Asadi, "Leached caps mineralogy and geochemistry as supergene enrichment fertility indicators, Meiduk and Parkam porphyry copper deposits, SW Iran," *J. Geochemical Exploration*, vol. 194, pp. 198–209, 2018.
- [66] H. Mirnejad, R. Mathur, J. Hassanzadeh, B. Shafie, and S. Nourali, "Linking Cu mineralization to host porphyry emplacement: Re–Os ages of molybdenites versus U–Pb ages of zircons and sulfur isotope compositions of pyrite and chalcopyrite from the Iju and Sarkuh porphyry deposits in southeast Iran," *Econ. Geol.*, vol. 108, no. 4, pp. 861–870, 2013.
- [67] M. Golestani, M. H. Karimpour, A. M. Shafaroudi, and M. R. H. Shahri, "Geochemistry, U–Pb geochronology and Sr–Nd isotopes of the neogene igneous rocks, at the Iju porphyry copper deposit, NW Shahr-e-Babak, Iran," *Ore Geol. Rev.*, vol. 93, pp. 290–307, 2018.
- [68] A. Zarasvandi, M. Rezaei, J. G. Raith, S. Asadi, and D. Lentz, "Hydrothermal fluid evolution in collisional Miocene porphyry copper deposits in Iran: Insights into factors controlling metal fertility," *Ore Geol. Rev.*, vol. 105, pp. 183–200, 2019.
- [69] H. Fereydooni and S. Mojeddifar, "A directed matched filtering algorithm (DMF) for discriminating hydrothermal alteration zones using the ASTER remote sensing data," *Int. J. Appl. Earth observation geoinf.*, vol. 61, pp. 1–13, 2017.

- [70] S. Mojeddifar and M. Mavadati, "Integration of support vector machines for hydrothermal alteration mapping using ASTER data—case study: The northwestern part of the Kerman Cenozoic Magmatic Arc, Iran," *Int. J. Mining Geo-Eng.*, vol. 54, no. 1, pp. 45–50, 2020.
- [71] D. A. Singer, V. I. Berger, and B. C. Moring, "Porphyry copper deposits of the world: Database and grade and tonnage models," U.S. Geological Surv., Reston, VA, USA, USGS open-file report 2008-1155, 2008.
- [72] L. C. Rowan, R. G. Schmidt, and J. C. Mars, "Distribution of hydrothermally altered rocks in the Reko Diq, Pakistan mineralized area based on spectral analysis of ASTER data," *Remote Sens. Environ.*, vol. 104, no. 1, pp. 74–87, 2006.
- [73] J. Perelló, A. Raziq, and J. Schloderer, "The Chagai porphyry copper belt, Baluchistan province, Pakistan," *Econ. Geol.*, vol. 103, no. 8, pp. 1583–1612, 2008.
- [74] J. P. Richards, T. Spell, E. Rameh, A. Raziq, and T. Fletcher, "High Sr/Y magmas reflect arc maturity, high magmatic water content, and porphyry Cu \pm Mo \pm Au potential: Examples from the Tethyan arcs of central and eastern Iran and western Pakistan," *Econ. Geol.*, vol. 107, no. 2, pp. 295–332, 2012.
- [75] A. Raziq, R. M. Tosdal, and R. A. Creaser, "Temporal evolution of the western porphyry Cu–Au systems at Reko Diq, Balochistan, western Pakistan," *Econ. Geol.*, vol. 109, no. 7, pp. 2003–2021, 2014.
- [76] L. Zürcher et al., "Tectono-magmatic evolution of porphyry belts in the central Tethys region of Turkey, the Caucasus, Iran, western Pakistan, and southern Afghanistan," *Ore Geol. Rev.*, vol. 111, 2019, Art. no. 102849.
- [77] R. G. Schmidt, "Mineral reconnaissance in the Chagai district, Pakistan, using a four-dimensional vector method of digital classification of Landsat data," *US Geological Surv.*, Reston, VA, USA, 1980.
- [78] T. H. Kuhn, "Pipe deposits of the Copper Creek area, Arizona," *Econ. Geol.*, vol. 36, no. 5, pp. 512–538, 1941.
- [79] J. Guthrie and D. Moore, "The geology of the Copper Creek area, Bunker Hill mining district, Galiuro Mountains, Arizona," in *Proc. Porphyry Copper Symp. Ariz Geol Soc Dig.*, 1978, pp. 25–31.
- [80] E. D. Anderson, W. W. Atkinson, T. Marsh, and A. Iriondo, "Geology and geochemistry of the mammoth breccia pipe, copper creek mining district, southeastern Arizona: Evidence for a magmatic–hydrothermal origin," *Mineralium Deposita*, vol. 44, no. 2, pp. 151–170, 2009.
- [81] T. McCandless and J. Ruiz, "Rhenium-osmium evidence for regional mineralization in southwestern North America," *Science*, vol. 261, no. 5126, pp. 1282–1286, 1993.
- [82] N. G. Banks and M. H. Krieger, "Geologic map of the Hayden quadrangle, Pinal and Gila counties," *Arizona. US Geological Surv.*, Reston, VA, USA, 1977.
- [83] E. R. Force, "Laramide alteration of proterozoic diabase; a likely contributor of copper to porphyry systems in the dripping spring mountains area, southeastern Arizona," *Econ. Geol.*, vol. 93, no. 2, pp. 171–183, 1998.
- [84] C. A. Richardson, E. Seedorff, W. Pennell, and L. Garside, "Reconstruction of normal fault blocks in the Ann-Mason and Blue Hill Areas, Yerington district, Lyon county, Western Nevada," in *Proc. New Concepts Discoveries: Proc., Geological Soc. Nevada Symp.*, 2015, pp. 1153–1178.
- [85] L. C. Carter, B. J. Williamson, S. R. Tapster, C. Costa, G. W. Grime, and G. K. Rollinson, "Crystal mush dykes as conduits for mineralising fluids in the Yerington porphyry copper district, Nevada," *Commun. Earth Environ.*, vol. 2, no. 1, pp. 1–11, 2021.
- [86] F. Maldonado, R. W. Spengler, W. Hanna, and G. Dixon, "Index of granitic rock masses in the state of Nevada. Department of the interior," *US Geological Surv.*, Reston, VA, USA, 1988.
- [87] A. M. Thibodeau, D. J. Killick, S. L. Hedquist, J. T. Chesley, and J. Ruiz, "Isotopic evidence for the provenance of turquoise in the southwestern United States," *Bulletin*, vol. 127, no. 11–12, pp. 1617–1631, 2015.
- [88] A. Gilmer, J. Kyle, J. Connelly, R. Mathur, and C. Henry, "Extension of laramide magmatism in southwestern North America into Trans-Pecos Texas," *Geol.*, vol. 31, no. 5, pp. 447–450, 2003.
- [89] S. N. Frelinger, M. D. Ledvina, J. R. Kyle, and D. Zhao, "Scanning electron microscopy cathodoluminescence of quartz: Principles, techniques and applications in ore geology," *Ore Geol. Rev.*, vol. 65, pp. 840–852, 2015.
- [90] W. Zheng et al., "Geology of the Jiama porphyry copper–polymetallic system, Lhasa region, China," *Ore Geol. Rev.*, vol. 74, pp. 151–169, 2016.
- [91] W. Zheng et al., "Exploration indicators of the Jiama porphyry–skarn deposit, Southern Tibet, China," *J. Geochemical Exploration*, vol. 236, 2022, Art. no. 106982.
- [92] S.-J. Zheng, H. Zhong, Z.-J. Bai, Z.-K. Zhang, and C.-Q. Wu, "High-sulfidation veins in the Jiama porphyry system, South Tibet," *Mineralium Deposita*, vol. 56, pp. 205–214, 2021.
- [93] Y. Li, X.-H. Li, D. Selby, and J.-W. Li, "Pulsed magmatic fluid release for the formation of porphyry deposits: Tracing fluid evolution in absolute time from the Tibetan Qulong Cu–Mo deposit," *Geol.*, vol. 46, no. 1, pp. 7–10, 2018.
- [94] B. Xiao et al., "Highly oxidized magma and fluid evolution of Miocene Qulong giant porphyry Cu–Mo deposit, Southern Tibet, China," *Resource Geol.*, vol. 62, no. 1, pp. 4–18, 2012.
- [95] Y.-b. Hu et al., "The formation of Qulong adakites and their relationship with porphyry copper deposit: Geochemical constraints," *Lithos*, vol. 220, pp. 60–80, 2015.
- [96] M. Abrams, S. Hook, and B. Ramachandran, "Aster user handbook, version 2," *Jet propulsion Lab.*, vol. 4800, pp. 1–31, 2002.
- [97] A. A. Green, M. Berman, P. Switzer, and M. D. Craig, "A transformation for ordering multispectral data in terms of image quality with implications for noise removal," *IEEE Trans. Geosci. remote Sens.*, vol. 26, no. 1, pp. 65–74, Jan. 1988.
- [98] J. Inzana, T. Kusky, G. Higgs, and R. Tucker, "Supervised classifications of Landsat TM band ratio images and Landsat TM band ratio image with radar for geological interpretations of central Madagascar," *J. Afr. Earth Sci.*, vol. 37, no. 1–2, pp. 59–72, 2003.
- [99] Y. Ninomiya, "A stabilized vegetation index and several mineralogical indices defined for ASTER VNIR and SWIR data," in *Proc. IEEE Int. Geosci. Remote Sens. Symposium. Proc.*, 2003, pp. 1552–1554.
- [100] D. Hong, N. Yokoya, J. Chanussot, and X. X. Zhu, "An augmented linear mixing model to address spectral variability for hyperspectral unmixing," *IEEE Trans. Image Process.*, vol. 28, no. 4, pp. 1923–1938, Apr. 2018.



Usama Zidan received the B.Sc. degree in computer science with artificial intelligence from the University of Nottingham, Nottingham, U.K, in 2020. He is currently working toward the Ph.D. degree with a strong background in computer science with Birmingham City University, Birmingham.

His research focuses on computer vision, specifically in the areas of image classification and segmentation.



Hamdy A. El Desouky received the bachelor's degree in geology from Menoufia University, Shibin Al Kawm, Egypt, in 2000, the master's degree from Ghent University, Ghent, Belgium, in 2005, and the Ph.D. degree in economic geology from KU Leuven University, Leuven, Belgium, in 2009.

He is currently a Professor of applied geology with Galala University, Galala, Egypt, and Menoufia University. He is also the Director of the Petroleum and Mining Geology Program with Galala University and acts as Secretary for the Petroleum and Mineral

Resources Council within the Egyptian Academy of Scientific Research and Technology. He conducted postdoctoral research for five years at KU Leuven University. He has supervised numerous M.Sc. and Ph.D. students both in Belgium and Egypt. He has been involved in more than 35 research projects that primarily investigate the genesis of world-class ore deposits including the Central African Copperbelt, the largest and richest copper–cobalt province on Earth. He has authored or coauthored 75 scientific papers and actively participated in 25 international conferences worldwide. He possesses extensive expertise in the application of remote sensing, GIS, fluid inclusions, and isotope geochemistry within various fields of applied geology. His research focuses on economic geology and mineral exploration to accelerate green transition.

Dr. Desouky has been recognized for his contributions to geological sciences with multiple scholarships, grants, and prestigious awards, such as Egypt's First Class Award of Excellence, State Encouragement Award in Geological Sciences, and Menoufia University's Encouragement Award.



Mohamed Medhat Gaber received the Ph.D. degree in artificial intelligence from Monash University, Melbourne, Australia, in 2016.

He is currently a Professor in data analytics with the School of Computing and Digital Technology, Birmingham City University, Birmingham, U.K. He then held appointments with the University of Sydney, Camperdown, CSIRO, Canberra, and Monash University, all in Australia. Prior to joining Birmingham City University, he worked for the Robert Gordon University as a Reader in computer science and with the University of Portsmouth as a Senior Lecturer in Computer Science, both in the U.K. He has authored or coauthored more than 200 papers, coauthored three monograph-style books, and edited/coedited six books on data mining and knowledge discovery. His work has attracted well more than 9000 citations, with an H-index of 45. He was in the program committees of major conferences related to data mining, including ICDM, PAKDD, ECML/PKDD and ICML. He has also cochaired numerous scientific events on various data mining topics.

Dr. Gaber is recognized as a Fellow of the British Higher Education Academy (HEA). He is also a Member of the International Panel of Expert Advisers for the Australasian Data Mining Conferences. In 2007, he was the recipient of the CSIRO teamwork award.



Mohammed M. Abdelsamea received the Ph.D. (with Doctor Europaeus) degree in computer science and engineering from IMT-Institute for Advanced Studies, Lucca, Italy, in 2015.

He is currently a Senior Lecturer in Data and Information Science with the School of Computing and Digital Technology, Birmingham City University (BCU), Birmingham, U.K. He is also a Fellow of the British Higher Education Academy. Before joining BCU, he worked for the School of Computer Science with Nottingham University, Nottingham, Mechanochemical Cell Biology with Warwick University, Coventry, Nottingham Molecular Pathology Node (NMPN), and Division of Cancer and Stem Cells both with Nottingham Medical School, Nottingham, as a Research Fellow. In 2016, he was a Marie Curie Research Fellow with the School of Computer Science, Nottingham University. Before moving to the U.K., he worked as a Lecturer of Computer Science for Assiut University, Assiut, Egypt. He was also a Visiting Researcher with Robert Gordon University, Aberdeen, U.K. His main research interests include computer vision including: image processing, deep learning, data mining, and machine learning, pattern recognition, and image analysis.